Corrosion Science 190 (2021) 109696

Contents lists available at ScienceDirect

Corrosion Science

journal homepage: www.elsevier.com/locate/corsci

Highly porous Ti as a bone substitute: Triboelectrochemical characterization of highly porous Ti against Ti alloy under fretting-corrosion conditions

A.I. Costa [a,b,*], F. Viana [b,c,d], F. Toptan [a,e,f], J. Geringer [g]

[a] CMEMS-UMinho – Center of MicroElectroMechanical Systems – Universidade do Minho, Campus de Azurém, Guimarães, Portugal
[b] DEMM – Department of Metallurgical and Materials Engineering – Faculdade de Engenharia da Universidade do Porto, Portugal
[c] LAETA – Associate Laboratory of Energy, Transports and Aeronautics – Faculdade de Engenharia da Universidade do Porto, Portugal
[d] INEGI – Institute of Science and Innovation in Mechanical and Industrial Engineering – Porto, Portugal
[e] IBTN/Euro – European Branch of the Institute of Biomaterials, Tribocorrosion and Nanomedicine – Departamento de Engenharia Mecânica, Universidade do Minho, Campus de Azurém, Guimarães, Portugal
[f] Department of Materials Science and Engineering, Izmir Institute of Technology, 35430, Urla, Izmir, Turkey
[g] Université de Lyon, IMT Mines Saint-Etienne, Centre CIS, INSERM SainBioSE U1059, F-42023, Saint-Etienne, France

ARTICLE INFO

Keywords:
Porous Ti
Tribocorrosion
Fretting-corrosion
Fretting map

ABSTRACT

Highly porous Ti was investigated under fretting-corrosion conditions as a function of load and amplitude. To obtain a correlation between mechanical and electrochemical responses according to amplitude, a new representative master curve was suggested: the A ratio (dissipated energy over total energy) vs. 1st OCP drop that fitted well the fretting-corrosion behaviour. Fretting-corrosion mechanisms were presented and a fretting map was illustrated. There was a significant load- and amplitude-dependent response, showing gross slip and partial slip regimes can occur with expected OCP variations. The promising structure of highly porous Ti was preserved after 16 h of fretting-corrosion under severe solicitations.

1. Introduction

The elderly population is increasing and together with lack of proper physical activity resulting in trauma or disease, the rate of implants used is rising. Implants require long-term stability and rapid healing however the existing Ti-based implant materials do not meet completely the current expectation [1,2].

Macro-porosity in the Ti implant was presented as a beneficial way to reduce the biomechanical mismatch, in order to approach the value of Young's modulus of the implant to the one found in the bone. It also gives the opportunity of ingrowth of new bone tissue inside of the pores [3–5].

Depending on the target implant application that can be dedicated for dental, hip, craniofacial or mandible, the functional requirements and aesthetics aspects should be considered where the mechanical properties can change throughout the implant and consequently, the functionality requirements will be heterogeneous through the implant. Macro-porosity can be combined with dense regions in order to achieve an implant structure that will fulfil the specified requirements for every section. Porosity may promote high vascularization and direct osteogenesis while the dense structure may promote mechanical stability. For example, in the case of the hip, the head part should be dense while the stem may be partly porous. In the case of the mandible, the dental abutment should be a dense region while the body of the implant may have porosity [3,6–9]. These approaches, with tailored design, can lead to several complications due to the introduction of additional interfaces, which are subjected to various loading conditions and micro-motions.

The study of simultaneous wear and corrosion (tribocorrosion) is one of the most important aspects of load-bearing systems. A hip implant is affected by sliding contact between the femoral and the tibial or acetabular component and it is immersed in body fluids, therefore it is susceptible to tribocorrosion. There are micro-motions in the points of the implant fixation. On the other hand, dental implants are also exposed to cyclic micro-motions at the implant–abutment and implant–bone interfaces. These micro-motions are leading to debris and consequently to ions released by fretting-corrosion [2,10].

* Corresponding author at: CMEMS-UMinho – Center of MicroElectroMechanical Systems – Universidade do Minho, Departamento de Engenharia Mecânica, Campus de Azurém, 4800-058, Guimarães, Portugal.
E-mail address: a66848@alunos.uminho.pt (A.I. Costa).

https://doi.org/10.1016/j.corsci.2021.109696
Received 14 January 2021; Received in revised form 1 June 2021; Accepted 16 July 2021
Available online 21 July 2021

A very limited number of tribocorrosion studies on porous structures [11,12] have been published, leaving a lack of understanding of the evaluation of the contacts between porous-dense Ti-based structures. This work aims at investigating, to the best of the authors' knowledge for the first time, the triboelectrochemical consequences of the micro-movements between the highly porous Ti against Ti alloy structures under fretting-corrosion solicitations. The fretting-corrosion behaviour of highly porous Ti in foetal bovine serum solution was studied as a function of normal load and according to displacement amplitude.

2. Materials and methods

Powder metallurgy with space holder technique was used to produce highly porous Ti samples (Ø =12 mm). Angular shaped Ti powders (Grade 2, Alfa Aesar, D50 = 36 μm) and angular shaped urea particles (Scharlau, <500 μm), 50 $_{vol}$%, were prepared in a ball mill for 4 h at 130 rpm with alumina balls, in an argon atmosphere. Then the procedure continued with the pressing stage where a zinc stearate lubricated nitrided stainless steel die was used to uniaxially press the power blends under 350 MPa for 2 min. Then, green compacts were subjected to a thermal cycle for space holder removal, performed at 450 °C for 3 h under argon atmosphere. Afterwards, the sintering step was performed at 1100 °C, for 3 h under high vacuum (<10^{-5} mbar). Highly porous Ti was characterized by tomography using a Nanotom 180 (Phoenix|X-ray, GE) equipment, with an accelerating voltage of 160 kV and a current of 75 μA. The sample was scanned in continuous mode and 2000 projections were performed around 360° with an exposure time of 500 ms for each projection.

Ti alloy (Ti-6Al-4 V) samples were manufactured according to ASTM F136.

Fretting-corrosion tests were carried out at room temperature (25 ± 2 °C) in a normal air atmosphere using a fretting-corrosion set-up where a mechanical (hydraulic and electro-mechanical) part contains the samples and the fixing parts. The sensors, based on linear voltage displacements transducers (LVDT) or capacitive ones, control the actual displacement. Moreover, the tangential load, Ft, is registered with load transducer and the dissipated energy, surface of Ft vs. displacement, is calculated. The normal load is driven through the contact pressure highlighted in the modular junction. The drawback of some electromagnetic motors is related to the low tangential load that is applied compared with hydraulic machines (more details described elsewhere [13–15]). The schematic representation of the fretting-corrosion equipment was illustrated in Fig. 1a. Metal surfaces were electrically insulated from the experimental device. Porous Ti were insulated with blue silicone (Loctite SI 5926) and Ti alloy samples were electrically insulated with oxidized zirconium (Zircalloy) alloy plates and varnished (RSPRO 19-1480), exposing to the electrolyte the surfaces facing each other. The tests were performed during 57600 cycles, i.e. 16 h. The electrolyte used was foetal bovine serum (Biowest™) with a protein content of 30 g/L. The initial protein content of the fresh solution was 60 g/L diluted that was deionized with water to obtain a protein content of 30 g/L (each solution was sealed in an airtight container and stored in the refrigerator immediately after every test). 300 mL of foetal bovine serum solution was used for each test to ensure that the samples were fully submerged into the solution. Electrochemical data was continuously monitored with a potentiostat (Parstat 2263) connected to the device of fretting-corrosion. During electrochemical measurements, a three-electrode configuration was used with a highly porous Ti sample as working electrode and platinum and saturated calomel electrodes (SCE) as counter and reference electrodes, respectively. The protocol started with a cathodic polarization at −1 V_{SCE} for 5 min followed by open circuit potential (OCP) monitorization, before, during and after fretting solicitation.

A substantial range of loads (no load applied, 22.5, 42.5, 85, 127.5, 170 and 200 N) was applied where linear voltage displacement transducer sensors on the device were in charge of controlling a displacement of ± 10, 40, 70 and 100 μm sinusoidal displacement. Tests were repeated to a minimum of 3 times (5 times max.) to ensure the reproducibility for ±40 μm sinusoidal displacement. For the rest of the amplitudes under study, only one test per load was carried out in order to obtain a fretting map. For each test, new samples of porous Ti and Ti alloy were used. It was not possible to apply the higher loads (170 N and 200 N) when higher amplitudes (± 70 and 100 μm) were imposed because the tangential load limit exceeded the limit that the tangential transducer was able to measure.

The usual master curve used in tribology is wear volume vs. total dissipated energy [16,17]. Due to corrosion phenomena in solution, the wear volume is not only the consequence of some mechanical degradations (friction). This statement provides the opportunity to combine both effects, i.e. electrochemistry and mechanics. In order to build and suggest a new master curve for each amplitude under study according to the load, 1st OCP drop vs the A ratio (dissipated energy over total energy) was calculated. After 1 h of stabilization, fretting started and 1st OCP drop was obtained by the difference between the potential before and after fretting started. The schematic representation of the fretting-corrosion protocol was illustrated in Fig. 1b. The A ratio (dissipated energy over total energy) was obtained with a mean of the last hour under fretting solicitation. Dissipated energy is the area of every tangential load vs. imposed displacement cycle.

3D profilometry (NT9100 ex. Veeco, Bruker™) was used in order to obtain wear profile for all the samples under study. The morphological features of the fretted corroded zones were assessed using scanning electron microscopy (SEM, Zeiss™Supra 55, 20 kV of voltage). Special attention was paid on the conduction of the holder in order to avoid some electrical charges accumulation, especially on porous titanium that exhibits non uniform oxide films.

3. Results and discussion

Fig. 2 presented the three-dimensional tomographic reconstructions of highly porous Ti sample together with the optical microscope (OM) images of the top surfaces. Supplementary video obtained by tomographic analysis and Fig. 2 showed a general look of the macro-porosity of highly porous Ti structures, presented closed and open (interconnected) pores well distributed through the sample. This work is a follow up of previous works where porous Ti was characterized. While processing more samples for this study, the characterisation was

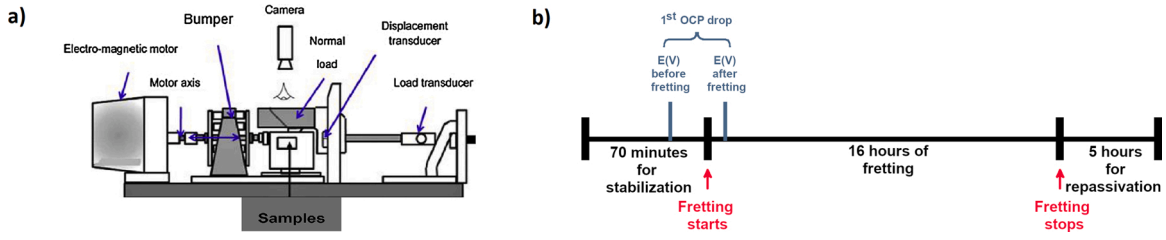

Fig. 1. Schematic representation of the fretting-corrosion a) equipment step-up and b) protocol.

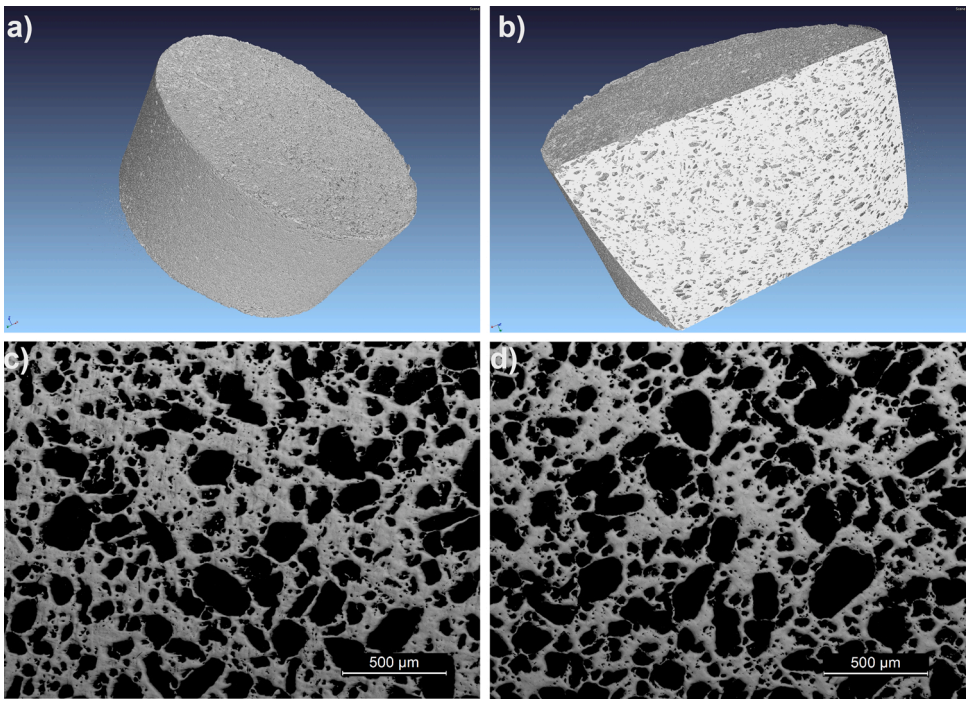

Fig. 2. Three-dimensional tomographic reconstructions of highly porous Ti sample with Ø =12 mm: a) top surface and b) cross-sectional view; c) and d) OM images from the top surface.

performed and the values were confirmed, proving reproducibility in the processing route. Induced (nominal) porosity was 50 %, but previous studies [18,19] with identical processing conditions showed that real porosity obtained by image analysis was around 37 %. About 80 % of the pores were in the range 50–350 µm, with an average pore size of around 200 µm [18,19].

Maximum Hertzian contact pressure for dense Ti/Ti alloy contact was calculated for all the loads under study (22.5, 42.5, 85, 127.5, 170 and 200 N) and results showed 210, 280, 400, 490, 570, 620 MPa respectively. A dense structure was assumed for contact pressure calculations, thus, it is reasonable to assume that the values during the tests were much higher due to reduced contact area because of porosity. These values of contact pressure were considerably above to the ones found in the human body for most of the cases in implant materials that are lower than 10 MPa [20–22]. For example, on the femoral structure (acetabulum cavity), the peak pressure for normal walking can be 3.26 MPa while standing up is 8.97 MPa [23].

Micro-movements occurring during the healing phase may lead to fibrous encapsulation of the implant and usually, they were in the range 3–50 µm, showed a maximum displacement of 71.9 µm [24–29]. According to this, 0.08 mm of displacement amplitude was investigated and representative curves from the results regarding fretting-corrosion tests for 16 h were presented in Fig. 3. Coefficient of friction (COF) values presented in Fig. 3a, showed a trend since values were decreasing with the increase of the load, with the exception for 127.5 N. For lower loads, 22.5 and 42.5 N, oscillations can be seen during the 16 h of the tests. On another way, for the rest of the loads, the COF was relatively stable through the duration of the test. The decreasing of the COF values, while the load was increasing, may be related with several factors, creating a complex system under study, where lubrication by the electrolyte, tribolayer formation and adhesive wear from the metal/metal contact can contribute. For instance, highly porous Ti presented protrusions that may be flattened while the load was increasing, promoting a decreased of COF. In order to evaluate tribocorrosion and fretting-corrosion behaviours as well as wear damages, COF evolution is widely used but following the results, in this study, an isolated COF evolution did not present a valuable contribution regarding fretting regimes and their transition. In this work, COF evolution was considered to compare the behaviour between the loads under study.

The representative curves for the evolution of OCP with time during fretting solicitations were presented in Fig. 3b. These OCP values were mixed potential values of highly porous Ti and Ti alloy, as well, mixed potential values of both the active (worn) and passive (unworn) surfaces of both materials. Highly porous Ti consisted of a mixture of open and closed pores (as presented in Fig. 2) and previous 3D reconstructions samples [18] showed that electrolyte can cross completely the samples. Although samples were isolated to prevent leaking of the electrolyte, a more extensive metallic area from the porous samples was exposed to the electrolyte than from Ti alloy. When fretting solicitations were starting, a decrease in the potential was observed for all the loads under study. The highest OCP drop was related to the test under 22.5 N indicating a higher perturbation of the native oxide film and more exposure of the underlying metal surface to the electrolyte. After fretting stopped, all samples recovered their potential values up to the ones registered before fretting soliciting. This may indicate that the repassivation process and growth of the oxide film happened once fretting finished.

Depending on the applied load, different characteristics are highlighted between the conditions in the acquired fretting hysteresis loops (tangential load vs. displacement) as observed in Fig. 3c and d. While fretting-corrosion was occurring, modifications of the contact parameters were happening depending on the load, and consequently, fretting hysteresis loops presented a dynamic response [30]. In this way, the response at cycle 10, correspondent to 3 h and 20 min of fretting solicitations (Fig. 3c) and cycle 240, correspondent to 16 h of fretting solicitations (Fig. 3d) were presented in order to show the main differences in the evolution between the fretting hysteresis loops at the beginning and the end of the experiments, respectively. While 22.5 N was being applied, gross slip was occurring for all the cycles. This behaviour was promoted by a contact that was characterised by a constant friction force associated with a pure dissipative behaviour and that was why the fretting hysteresis loops presented a quadratic shape [31]. For 42.5, 85, 127.5, 170 and 200 N fretting hysteresis loops, an elliptic shape was obtained. However, for 42.5 N, the final loop presented a different shape than the one presented in the beginning, and that can

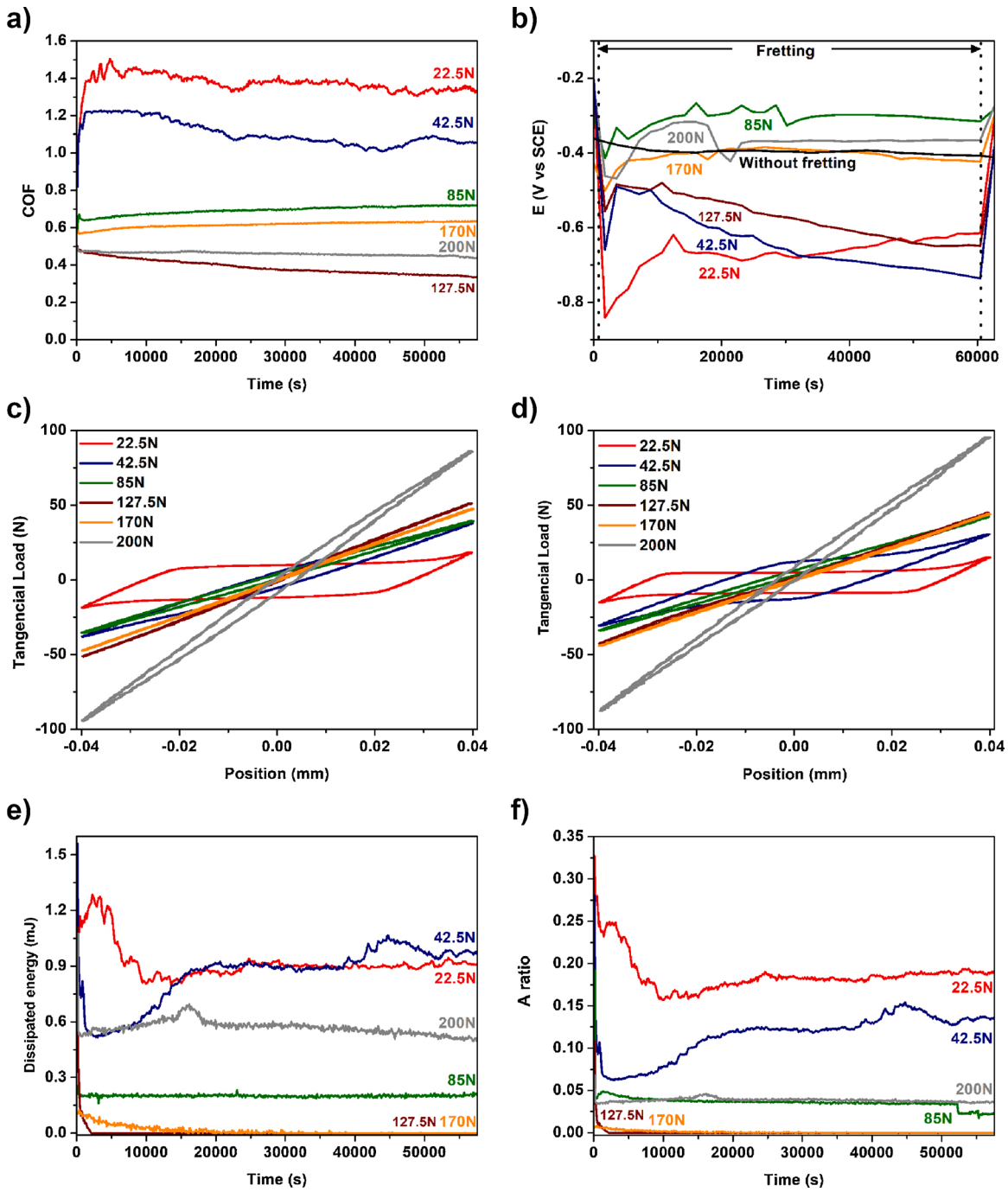

Fig. 3. a) Coefficient of friction evolution, b) open circuit potential evolution; c) representative fretting hysteresis loops (tangential load vs displacement) for cycle 10 and d) for cycle 240; e) dissipated energy evolution and f) the A ratio evolution between Ti alloy vs highly porous Ti under fretting-corrosion tests for several loads with 0.08 mm of displacement amplitude.

mean a mixed slip regime, starting with partial slip and then became more close to a gross slip regime [31]. The difference in the values of dissipated energy presented in Fig. 3e is a consequence related to the shape of the hysteresis loops due to the difference in the fretting regimes. 22.5 N and 42.5 N presented hysteresis loops with a quadratic shape that consequently expressed in high values of dissipated energy. 200 N presented a hysteresis loop with a bigger area than intermediate loads (85, 127.5 and 170 N) and consequently higher dissipated energy was obtained for 200 N. When the dissipated energy obtained is around 0 (like it was obtained for 85, 127.5 and 170 N), adhesion and partial slip are preponderant phenomena due to changes in the mechanical degradation. Fretting regimes can also be characterized by the ratio obtained between the dissipated energy over the total energy called the A ratio [15]. This energy ratio, defined by Mindlin and Deresiewicz [32] approach, followed by Fouvry et al. [17], allows accessing the transition between partial and gross slip regimes. If the A ratio (in a cylinder vs. plane contact) is below 0.2, a partial slip regime is occurring as presented by Fig. 3f for 42.5, 85, 127.5, 170 and 200 N. For 22.5 N, it was possible to see that the first cycles were under a gross slip regime (energy ratio $>$ 0.2), in accordance with the fretting hysteresis loops shown in Fig. 3c, followed by a transition for the partial slip regime. On the other hand, 42.5 N presented an evaluation of the A ratio that followed the opposite trend, showing lower values, in the beginning, increasing the values at the end of the test, being closer to a gross slip regime, as in

accordance with the fretting hysteresis loops presented in Fig. 3d.

Worn surfaces of highly porous Ti and Ti alloy were evaluated by SEM and optical profilometry and representative images for the respective loads under study were given in Figs. 4 and 5, respectively. Highly porous Ti worn surfaces presented parallel sliding grooves due to abrasive wear together with the compacted oxidized wear debris. From 22.5 to 200 N, the deepness of the grooves and the small particles as wear debris seemed to be decreased, suggesting that at lower loads, friction was more efficient. This may be linked with COF evolution, where 22.5 N presented the highest COF values (Fig. 3a). With the entrapment of the wear debris, adhered and dense oxidized patches on the worn surfaces were getting thicker, surface roughness was consequently getting higher, leading to higher COF values. At 127.5 N, Fig. 4a presented a decrease in the number of noticeable grooves, showing the

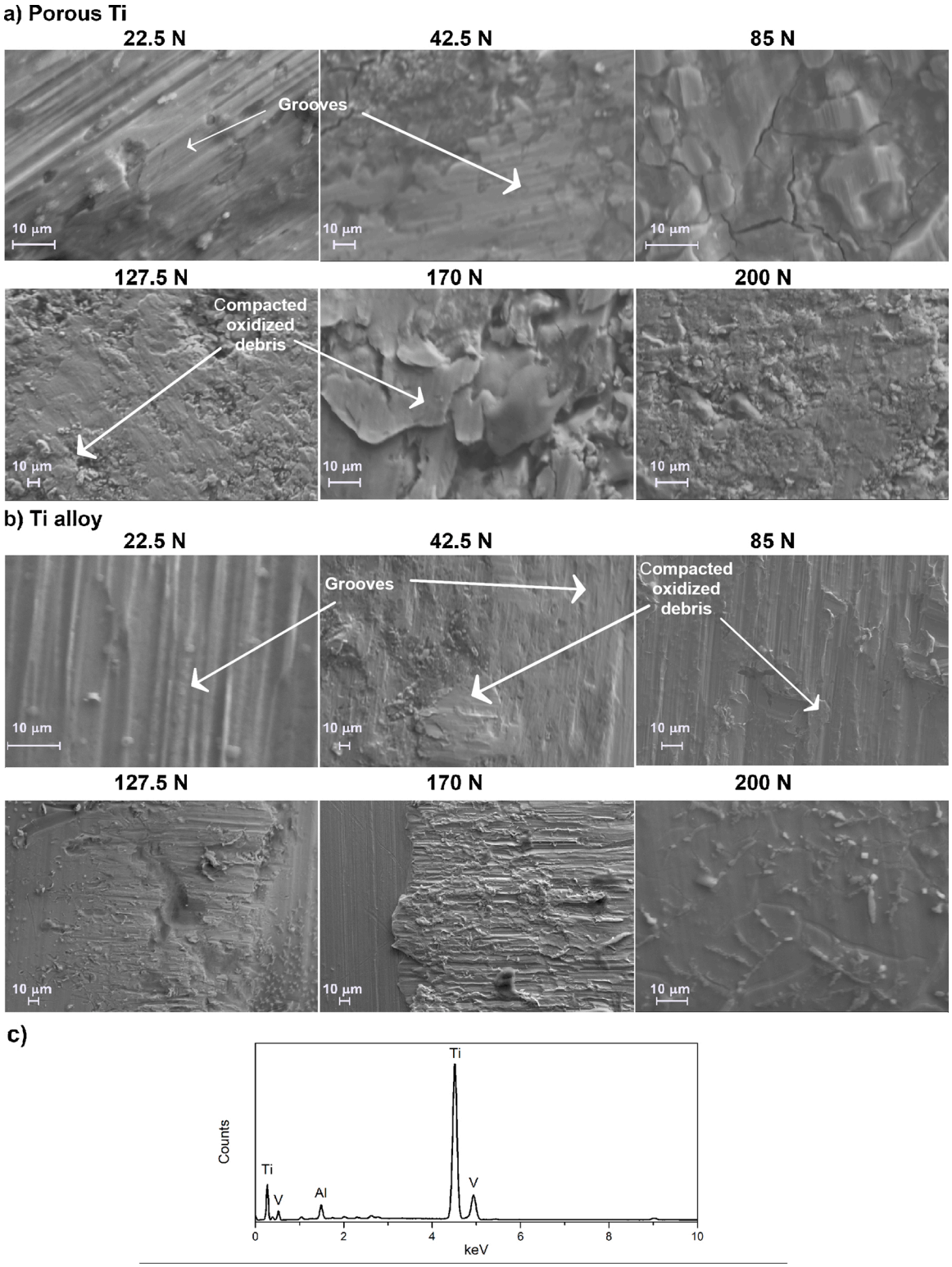

Fig. 4. SEM images of a) highly porous Ti and b) Ti alloy worn surfaces for several loads with 0.08 mm of displacement amplitude; c) EDS spectrum obtained in the wear tracks of highly porous Ti.

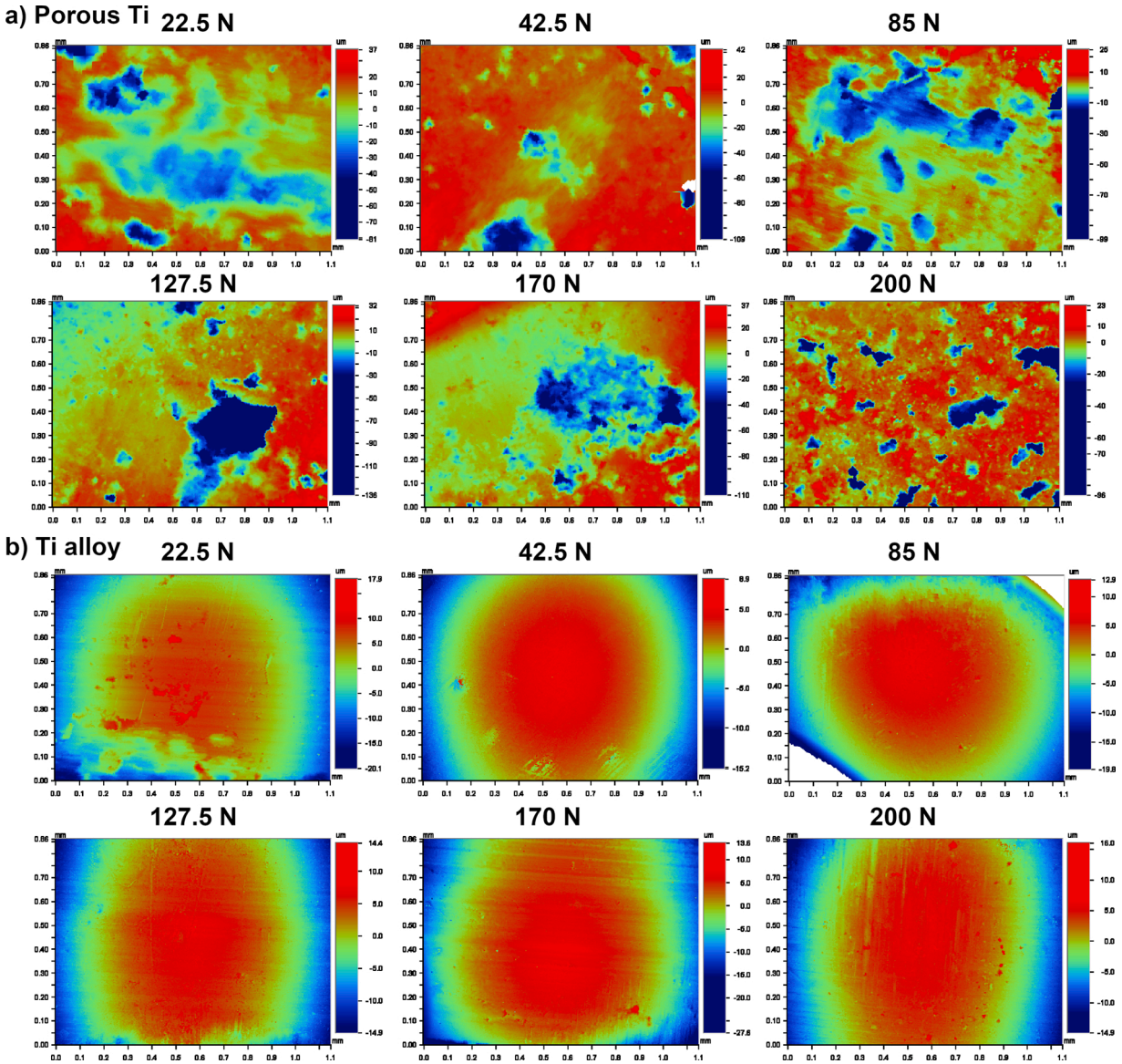

Fig. 5. Worn surfaces images by optical profiles for a) highly porous Ti and b) Ti alloy for several loads with 0.08 mm of displacement amplitude.

smoothing of the porous structures. At 200 N, less visible degradation was noticed, pointing that a sort of polishing and smoothing of the surface occurred due to partial slip behaviour.

Macro-pores presented loose oxidized wear debris. On porous structures, wear debris generated can go inside of the pores and can be compacted. In this way, the ejection of the wear debris into the pores can decrease the third-body abrasion that also contributed to an improved tribocorrosion performance [12].

In accordance with what was noticed in the highly porous Ti wear tracks, Ti alloy presented grooves more pronounced at lower loads, as presented in Fig. 4b. At 22.5 N, this phenomenon was well visible, decreasing at 42.5 N where just low marks and slightly less marked grooves were visible. SEM image presented for Ti alloy at 42.5 N represented the mixed slip regime discussed above in Fig. 3 since the bottom part of the wear track showed signs of sticking and adhesion while the rest showed a slip mechanism. At 200 N, no grooves were visible together with no substantial marks, proving an idea of sticking mechanism with small friction. At 200 N, Ti alloy surfaces presented only crystals precipitated from the electrolyte showing no wear debris formation. Ti alloys worn surfaces presented more distinguished parallel sliding grooves than porous Ti and it was previously stated that wear tracks were less noticeable in porous Ti structures than in dense structures when tribocorrosion tests were performed against a ceramic material [12]. The same trend was found for the compacted wear debris or tribolayer. These oxides compacted in a layer can play a protective role by reducing the wear due to adhesive wear, but they can also be freely moving in the electrolyte and/or they can work as third body wear. Under fretting solicitations, wear particles can also become entrapped in the fretted regions, in this way they can work as load-carrying plateau [33,34].

The fretting response from the material is linked with a regime characterized by its mechanisms of surface degradation and wear track. For example, the partial slip regime is usually associated with few amounts of wear. The explanation is the low dissipated energy produced during the test where some parts of the contact remain adhered to each other and no relative motion takes place between them. Consequently, there is no wear. In this regime, only a smaller part of the contact experiences relative motion (thus low dissipated energy). Partial slip regime can be divided into two main domains: a security domain without damage and a domain where cracking appears. Usually, cracking first appears under partial slip conditions, whereas the material removal and the debris formation are mainly encountered under large

displacement conditions. Gross slip regime is characterized by a high dissipated energy due to the sliding phenomena that occurs between the surfaces of the contacting bodies. Gross slip regime usually presents severe surface damage by wear due to significant material removal, with a lot of third body effects while mixed slip regime generates competition between cracking and wear [31,35,36].

EDS analysis, presented in Fig. 4c, detected some Al and V elements in the composition of porous Ti worn surfaces, from the Ti-6Al-4V counter-face, supporting the transfer mechanism between highly porous Ti and Ti alloy. During fretting of Ti structures, multiple wear mechanisms, such as adhesive, abrasive and oxidative wear, can occur sequentially or simultaneously. Ti structures are characterised by high adhesion, severe adhesive wear and high-and-unstable friction when sliding against nearly any other material. It is known that Ti structures have a high tendency for adhesion which causes sticking. Under dynamically loaded conditions, severe adhesive wear may occur when Ti slides against Ti, creating a lot of debris. Adhesion occurs in the case of direct contact between two metallic surfaces. If the distance between the two surfaces is in the order of the interatomic distance of the metal lattice, metallic bonds have established that cross the gap between both surfaces. When the surfaces move on, these new bonds often prevail and fracture occurs at some distance to the surface, leading to so-called fretting. The surface roughness, as well as oxide layers on top of the surfaces, normally hinder direct metallic contact. Plastic deformation of the surface, however, can lead to a flattening of roughness as well as to cleavage of oxide surface layers. The mechanism of adhesive wear describes the transference between sliding surfaces that are in very close proximity of soft material to a harder mating counter-face. It is caused by the solid-phase welding of asperities and when sliding is continuous, these junctions shear causing the material to be transferred. The formation of the transfer film is governed by the counter-face material, surface roughness and sliding conditions [37–39]. At the regions of real contact, strong adhesion or cold-welding occurs and the friction force is essentially the force required to shear the junction formed. With sliding motion present, junction growth occurs and eventually, junction shearing takes place. As sliding continues, fresh junctions will form and be ruptured in turn. If the adhesive strength is stronger than the cohesive strength of either of the two materials, then the junction will rupture within the weaker asperity. As a result, the material is transferred from one surface to the other and some are eventually detached to form loose wear particles. By contrast, if the process of damaging the oxide film predominates, then the wear becomes worse and severe wear takes place, characterised by surface roughening and coarse metallic debris [37–39]. In this way, adhesive wear is a very serious form of wear characterized by high wear rates and a large unstable COF, supported by the COF values presented in Fig. 3a for lower loads under study for 0.08 mm of displacement amplitude.

A smoothing of the porous structure can also be detected in Fig. 5. On the wear profiles of the porous structures, it was noticed material compaction and as well wear debris inside of the macro-pores, as can be seen in Fig. 5a, for 170 N condition represented by the green isolated zones inside of the big pore coloured in blue. Highly porous Ti structures exhibited a damaged surface represented by the green parts, surrounded by a less damaged zone coloured in red, except for 200 N. Parallel grooves for all Ti alloy images were highlighted by the optical profiles depicted in Fig. 5b, following what was discussed above in Fig. 4b. Once again, sticking phenomena was highlighted at 200 N, since highly porous Ti profiles showed less damage and Ti alloy profiles presented less pronounced grooves.

The surface morphology of the highly porous Ti was preserved after 16 h of fretting-corrosion for all the loads under study: no destruction of the structure, low wear, few/no grooves and a porous structure highlighted. As a result of microscopical and profilometric observations, together with electrochemical and fretting analysis, a proposed fretting-corrosion mechanism of highly porous Ti against Ti alloy is illustrated in Fig. 6. Due to the reduced contact area of the macro-porous surfaces, higher contact pressures were obtained on the contact zones leading to more severe local damage, where the most pultruded zones of the porous structures were flattened, creating wear debris. These new wear debris that were generated can be work-hardened, and/or can be mixed with the oxidized wear debris (third-bodies). Consequently, wear debris can be compacted on the worn surfaces, forming oxidized patches, whereas some of these debris may adhere on counter-body surfaces that can abrade the metal leading to the formation of grooves on the worn surfaces or move freely on the sliding surfaces, acting as third-body particles (Fig. 6), or can go inside of the pores. Compacted oxidized debris in Fig. 5 supports the transfer mechanisms and transferred material is illustrated in Fig. 6. For porous structures, as the load was decreasing, it seemed that the severity of abrasive wear increased. In the literature, under the conditions most similar to this work, the contribution of corrosion on the wear is minimal, and the dominant degradation mechanism is mechanical wear [40–42].

The focus of this study was to evaluate, to the best of the authors' knowledge for the first time, the tribocorrosion behaviour of highly porous Ti against Ti alloy, simulating fretting-corrosion interfaces of implants. Depending on the load and the amplitude imposed, highly

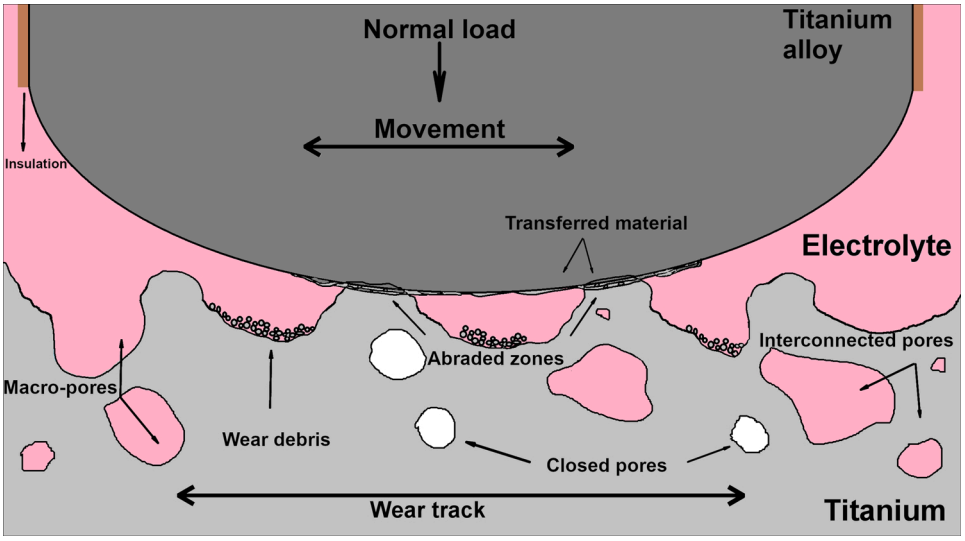

Fig. 6. Schematic draw of the suggested fretting-corrosion mechanisms for highly porous Ti against Ti alloy.

porous Ti against Ti alloy can present a different behaviour. In order to obtain a correlation between the mechanical and electrochemical responses according to the displacement amplitude [43], Fig. 7 presented the evolution of the 1st OCP drop when fretting started according with the A ratio. 0.02 mm as displacement amplitude was characterized by low values of the 1st OCP drop and low values of the A ratio, as presented in Fig. 7a, showing a partial slip behaviour for all the loads under study. No significant differences can be seen between all the loads under study. In accordance with Fig. 3, for 0.08 mm as displacement amplitude, Fig. 7b presented that the biggest drop on OCP under fretting was the test with the extreme minimum load under study, 22.5 N, followed by 42.5 N condition. Fretting micro-motions at lower load (22.5 N) induced gross slip with high and unsteady COF values (Fig. 3a), and presented a big OCP drop when fretting was applied (Fig. 3b), supported by hysteresis loops (Fig. 3c and d) with quadratic shape, that consequently expressed in high values of dissipated energy (Fig. 3e). The A ratio (Fig. 3f) allowed accessing that during the test, a regime transition may occur from gross slip to partial slip. Under 42.5 N, a mixed slip regime was presented, with contrary behaviour of the previous one described. According to hysteresis loops (Fig. 3c and d), response started with partial slip and with time, the behaviour became closer to the gross slip regime, supported by the A ratio evolution (Fig. 3f), presenting high values for dissipated energy (Fig. 3e). For higher loads (85, 127.5, 170 and 200 N), most of the dissipated energy (Fig. 3e) decreased back to near zero that together with the A ratio (Fig. 3f), showed that with higher loads the response becomes more robust showing to be in a partial slip regime. No significant differences can be seen between 85, 127.5, 170 and 200 N, showing a similar response under fretting-corrosion at the interface highly porous Ti against Ti alloy, characterizing a partial slip behaviour. For 0.14 mm, the values obtained for the loads that were possible to study, presented in Fig. 7c, showed a shift for the right side of the graph. 42.5 N presented a mixed slip regime while the rest of the load presented a partial slip regime. The transition from partial to gross slip was occurring around 0.14 mm, presenting this displacement amplitude as a threshold of the fretting-corrosion behaviour. Regarding tests with an amplitude imposed of 0.2 mm, presented in Fig. 7d, all the loads were shifted for a higher A ratio, in comparison with the values obtained for the other amplitudes under study, except for 22.5 N. This high A ratio obtained showed a gross slip behaviour for all the loads under this imposed amplitude.

Representative SEM images of highly porous Ti worn surfaces for 22.5 N with 0.02 mm of amplitude, 22.5 N and 42.5 N with 0.14 mm of amplitude were presented in Fig. 7e, f and g respectively. These images were chosen in order to represent the features correspond to partial slip (Fig. 7e and f) and gross slip regime (Fig. 7g), presented more noticeable

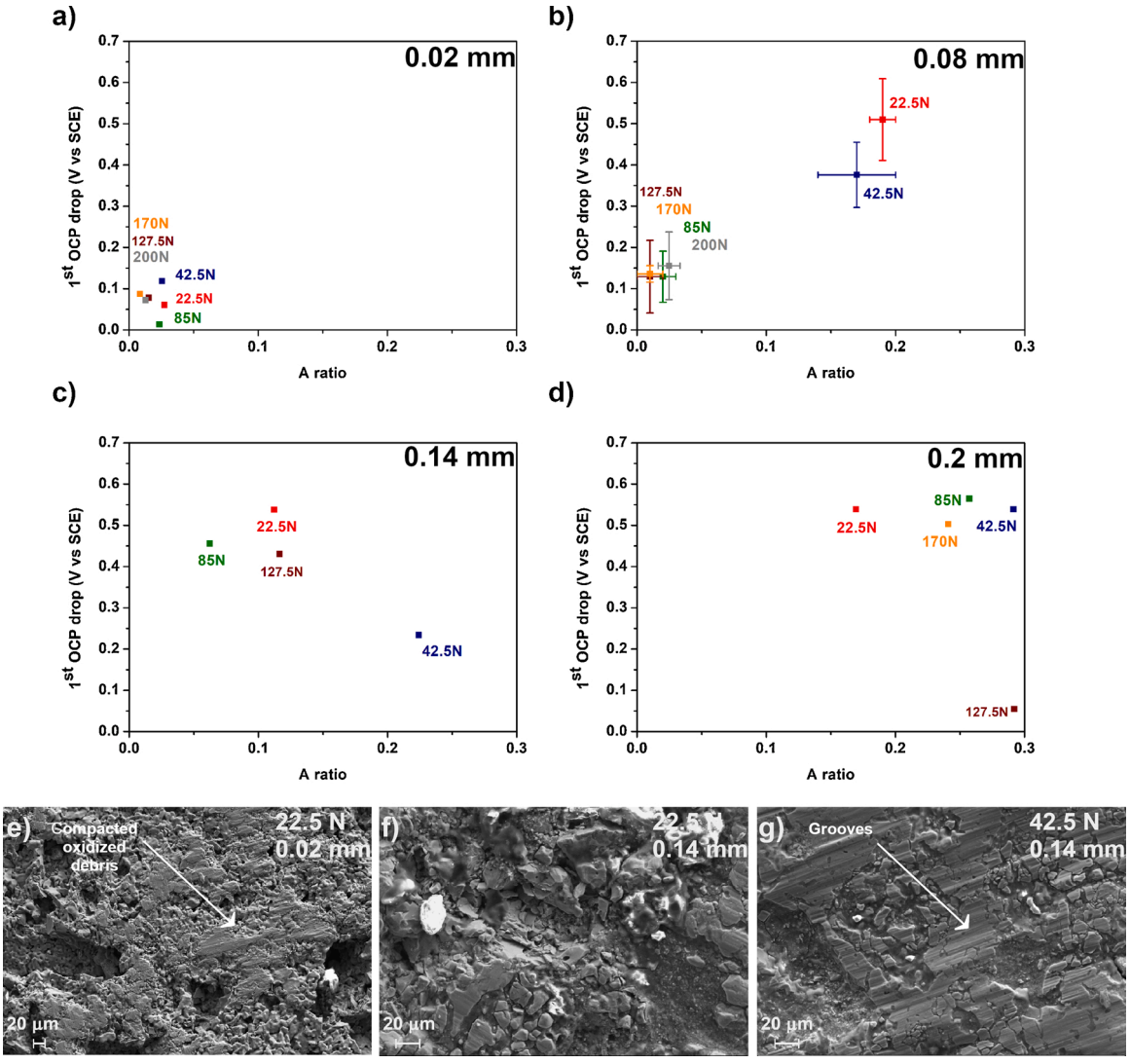

Fig. 7. Evolution of the 1st OCP drop when fretting started according to the A ratio for the displacement amplitudes imposed: a) 0.02, b) 0.08, c) 0.14 and d) 0.2 mm; SEM images of highly porous Ti worn surfaces for e) 22.5 N with 0.02 mm of amplitude, f) 22.5 N and g) 42.5 N with 0.14 mm of amplitude.

grooves. With the increase of the displacement amplitude, gross slip regime started to be established and consequently, one may assess the COF decreased by wear, which generated a compliant third body layer together with higher worn material removal and a shorter crack length [31,35,36].

This study presented an amplitude and load-dependent responses under fretting-corrosion solicitations between highly porous Ti and Ti alloy. Fig. 7 allowed the construction of a schematic illustration of a fretting map in terms of contact load and displacement amplitude obtained regarding the consequences of the micro-movements between highly porous Ti against Ti alloy, presented in Fig. 8. A fretting map is a diagram showing the relevant regimes in two variables, with regime boundaries representing critical values for the transition from one regime to another [36]. The obtained fretting map was in accordance with [44,45], where partial slip was followed by a mixed slip regime and then gross slip for higher displacement amplitudes.

Open circuit potential with the mechanical data from the tangential force and displacement analysis can provide information about the properties and behaviour of materials during fretting-corrosion tests. However, there were several limitations to this study. Firstly, for 0.02, 0.14 and 0.2 mm of displacement amplitude, only one test was performed for each load under study. In this way, a number of repetitions need to be performed in order to verify the proposed fretting map. Secondly, in the literature, master curves are presented using with the evolution of the wear rate or wear volume according to the cumulated dissipated energy [16,17,45,46], however when evaluating tribocorrosion behaviour of porous materials, this approach was not viable since it was difficult to distinguish a pore with wear damage. Besides, wear debris may go inside the pores and/or being compacted inside the pores, misguiding wear or weight loss measurements. However the A ratio vs. 1st OCP drop seems to make sense according to the tribological behaviour. Thirdly, in order to use this contact geometry approach, dense-on-porous contact, it was difficult to calculate the accurate real contact pressure. Actually, due to the surface roughness, the real contact between two counter-parts was composed of many small asperity contacts. In lubricated conditions like in this study, the hydrodynamic film may stay in these small junctions and carries part of the applied normal force. In this way, the actual force applied will be reduced comparing to non-lubricated condition where the total applied normal force was carried solely by the contacting asperities [47]. Since one of the counter-parts was a porous structure, it was possible that at the start of the tests, only some points were in contact, mainly due to the existence of pores. Afterwards, with the destruction of the top of the porous structure, the contact area was increasing which may lead to underestimation of the contact pressure as the porous Ti material was degraded, giving relatively lower contact pressure at the end of the test.

Even so, this study provided, to the best to the authors' knowledge, a first insight on the evaluation of porous Ti material under fretting-corrosion solicitations. These results can support the next investigations with the aim to evaluate the viability of this material for potential use in orthopaedic implants. Nevertheless, there is a need for generic standards that deal with fretting as well as test standards for specific devices [44], and these results showed that a new master curve of the A ratio vs. 1st OCP drop may be promising to study and to evaluate such complex systems.

Further investigations should focus on fatigue corrosion evaluation to study how porous Ti materials behave with crack initiation and propagation during cyclic stresses that can lead to the creation of new non-passivated surfaces in the metallic structures. Further investigations should also evaluate the synergism between corrosion and wear during fretting corrosion tests. It should be noted that in future studies that the study of corrosion in dynamic fluids containing proteins and microorganisms that can affect the electrochemical and triboelectrochemical response of porous materials is crucial, to mimic the *in vivo* conditions.

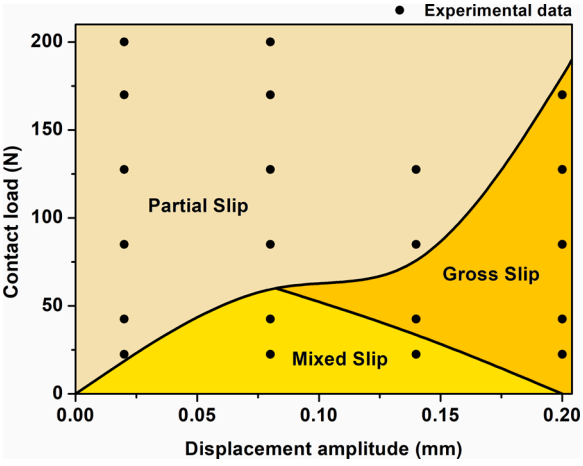

Fig. 8. Schematic illustration of a fretting map in terms of contact load and displacement amplitude obtained regarding the consequences of the micro-movements between highly porous Ti against Ti alloy.

4. Conclusions

This study complies the characterization of highly porous Ti as a potential bone substitute under fretting solicitations.

The fretting response was highly dependent on the applied load and several mechanical responses were obtained, from gross slip under low normal load until partial slip under high loads.

In order to obtain a correlation between the mechanical and electrochemical responses according to displacement amplitude, a new representative master curve was suggested: the A ratio vs. 1st OCP drop. 0.02 mm as displacement amplitude was characterized by low values of 1st OCP drop and low values of the A ratio, showing a partial slip behaviour for all the loads under study. For 0.08 mm of displacement amplitude, 22.5 N presented gross slip regime, 42.5 N a mixed slip regime and the rest of the loads presented partial slip regime. 0.14 mm was presented as a threshold amplitude for behaviour because tests with 0.2 mm, presented higher A ratio, shifting the behaviour for gross slip regime. A fretting map was built in terms of contact load and displacement amplitude regarding the consequences of the micro-movements between highly porous Ti against Ti alloy.

The surface morphology of the highly porous Ti was mostly preserved after 16 h of fretting-corrosion solicitations. The benefits of porous titanium seem promising for replacing some metallic parts well used in dentistry and implants field.

Author's contribution

Author's detailed description of their diverse contributions to the published work are given below:

A.I. Costa: Conceptualization (equal), Data curation (lead), Methodology (equal), Validation (equal), Formal analysis (lead), Investigation (equal), Writing - original draft (lead), Visualization (lead), Funding acquisition (supporting).

F. Viana: Writing - review & editing (supporting), Supervision (equal), Project administration (lead), Funding acquisition (lead).

F. Toptan: Conceptualization (equal), Methodology (equal), Validation (equal), Writing - review & editing (lead), Supervision (equal), Project administration (lead), Funding acquisition (lead).

J. Geringer: Conceptualization (equal), Methodology (equal), Validation (equal), Investigation (equal), Resources (lead), Writing - review & editing (lead), Supervision (equal), Project administration (supporting).

All authors discussed the results and contributed to the final manuscript.

Declaration of Competing Interest

The authors declare that they have no known competing financial interests or personal relationships that could have appeared to influence the work reported in this paper.

Acknowledgements

The authors would like to thank Mr. Albert Boyer for machining the Ti alloy samples, Ms. Maryline Mondon for the assistance in the SEM investigations and Mr. Olivier Valfort for the tomography analysis. This work was a result of the project Operation NORTE-08-5369-FSE-000051 supported by Norte Portugal Regional Operational Program (NORTE 2020), under the PORTUGAL 2020 Partnership Agreement, through the European Social Fund (ESF) and M-ERA-NET/0001/2015 project supported by FCT. This work was also supported by FCT national funds, under the national support to R&D units grant, through the reference project UIDB/04436/2020 and UIDP/04436/2020.

Appendix A. Supplementary data

Supplementary material related to this article can be found, in the online version, at doi:https://doi.org/10.1016/j.corsci.2021.109696.

References

[1] M. Geetha, A.K. Singh, R. Asokamani, A.K. Gogia, Ti based biomaterials, the ultimate choice for orthopaedic implants – a review, Prog. Mater. Sci. 54 (2009) 397–425.
[2] J. Villanueva, L. Trino, J. Thomas, D. Bijukumar, D. Royhman, M.M. Stack, M. T. Mathew, Corrosion, tribology, and tribocorrosion research in biomedical implants: progressive trend in the published literature, J. Bio- Tribo-Corros. 3 (2017).
[3] A. Bansiddhi, D.C. Dunand, Titanium and NiTi Foams for Bone Replacement, Woodhead Publishing Limited, 2014.
[4] A. Nouri, Titanium foam scaffolds for dental applications, Met. Foam Bone (2017) 131–160.
[5] A.C. Alves, R. Thibeaux, F. Toptan, A.M.P. Pinto, P. Ponthiaux, B. David, Influence of macroporosity on NIH/3T3 adhesion, proliferation, and osteogenic differentiation of MC3T3-E1 over bio-functionalized highly porous titanium implant material, J. Biomed. Mater. Res. - Part B Appl. Biomater. 107 (2019) 73–85.
[6] A. Kumar, K. Biswas, B. Basu, Hydroxyapatite-titanium Bulk Composites for Bone Tissue Engineering Applications, 2014, pp. 1–16.
[7] F.A. España, V.K. Balla, S. Bose, A. Bandyopadhyay, Design and fabrication of CoCrMo alloy based novel structures for load bearing implants using laser engineered net shaping, Mater. Sci. Eng. C 30 (2010) 50–57.
[8] J. Parthasarathy, B. Starly, S. Raman, A design for the additive manufacture of functionally graded porous structures with tailored mechanical properties for biomedical applications, J. Manuf. Process. 13 (2011) 160–170.
[9] C. Simoneau, P. Terriault, B. Jetté, M. Dumas, V. Brailovski, Development of a porous metallic femoral stem: design, manufacturing, simulation and mechanical testing, Mater. Des. 114 (2017) 546–556.
[10] K.T. Sipek, M.E. Lyvers, M.T. Mathew, Failure causes in total hip replacements: a review, Austin J. Orthop. Rheumatol. 5 (2018) 1064.
[11] A.I. Costa, L. Sousa, A.C. Alves, F. Toptan, Tribocorrosion behaviour of bio-functionalized porous Ti surfaces obtained by two-step anodic treatment, Corros. Sci. 166 (2020), 108467.
[12] F. Toptan, A.C. Alves, A.M.P. Pinto, P. Ponthiaux, Tribocorrosion behavior of bio-functionalized highly porous titanium, J. Mech. Behav. Biomed. Mater. 69 (2017) 144–152.
[13] L. Semetse, B.A. Obadele, L. Raganya, J. Geringer, P.A. Olubambi, Fretting corrosion behaviour of Ti-6Al-4V reinforced with zirconia in foetal bovine serum, J. Mech. Behav. Biomed. Mater. 100 (2019), 103392.
[14] J. Geringer, D.D. Macdonald, Friction/fretting-corrosion mechanisms: current trends and outlooks for implants, Mater. Lett. 134 (2014) 152–157.
[15] J. Geringer, V. Fridrici, H. Ding, K. Kim, T. Taylor, L. Semetse, S. Ehsani-majd, P. Olubambi, J. Fontaine, P. Kapsa, Some hard or soft coatings to protect the pristine biometallic substrates under fretting-corrosion solicitations: what should be the best solution? Lubricants 8 (2020) 1–14.
[16] S. Fouvry, P. Kapsa, An energy description of hard coating wear mechanisms, Surf. Coat. Technol. 138 (2001) 141–148.
[17] S. Fouvry, P. Kapsa, H. Zahouani, L. Vincent, Wear analysis in fretting of hard coatings through a dissipated energy concept, Wear 203–204 (1997) 393–403.
[18] A.C. Alves, A.I. Costa, F. Toptan, J.L. Alves, I. Leonor, E. Ribeiro, R.L. Reis, A.M. P. Pinto, J.C.S. Fernandes, Effect of bio-functional MAO layers on the electrochemical behaviour of highly porous Ti, Surf. Coat. Technol. 386 (2020), 125487.
[19] A.C. Alves, I. Sendão, E. Ariza, F. Toptan, P. Ponthiaux, A.M.P. Pinto, Corrosion behaviour of porous Ti intended for biomedical applications, J. Porous Mater. 23 (2016) 1261–1268.
[20] G. Wang, W. Huang, Q. Song, J. Liang, Three-dimensional finite analysis of acetabular contact pressure and contact area during normal walking, Asian J. Surg. 40 (2017) 463–469.
[21] F. Mazoochian, A. Hölzer, J. Jalali, F. Schmidutz, C. Schröder, M. Woiczinski, J. Maierl, P. Augat, V. Jansson, Finite element analysis of the ovine hip: development, results and comparison with the human hip, Vet. Comp. Orthop. Traumatol. 25 (2012) 301–306.
[22] M.M. Ardestani, M. Moazen, Z. Chen, J. Zhang, Z. Jin, A real-time topography of maximum contact pressure distribution at medial tibiofemoral knee implant during gait: application to knee rehabilitation, Neurocomputing 154 (2015) 174–188.
[23] H. Yoshida, A. Faust, J. Wilckens, M. Kitagawa, J. Fetto, E.Y.S. Chao, Three-dimensional dynamic hip contact area and pressure distribution during activities of daily living, J. Biomech. 39 (2006) 1996–2004.
[24] M.K. Friedrich Graef, Determination of micromotion at the implant bone interface - an in-vitro methodologic study, Dentistry 5 (2015).
[25] M. Baxmann, S.Y. Jauch, C. Schilling, W. Blömer, T.M. Grupp, M.M. Morlock, The influence of contact conditions and micromotions on the fretting behavior of modular titanium alloy taper connections, Med. Eng. Phys. 35 (2013) 676–683.
[26] S.Y. Jauch, G. Huber, H. Haschke, K. Sellenschloh, M.M. Morlock, Design parameters and the material coupling are decisive for the micromotion magnitude at the stem-neck interface of bi-modular hip implants, Med. Eng. Phys. 36 (2014) 300–307.
[27] S. Holst, H. Geiselhoeringer, M. Wichmann, A.I. Holst, The effect of provisional restoration type on micromovement of implants, J. Prosthet. Dent. 100 (2008) 173–182.
[28] J.B. Brunski, In vivo bone response to biomechanical loading at the bone/dental-implant interface, Adv. Dent. Res. 13 (1999) 99–119.
[29] S.S. Moncler, H. Salama, Y. Reingewirtz, J.H. Dubruille, Timing of loading and effect of micromotion on bone–dental implant interface: review of experimental literature, J. Biomed. Mater. Res. 43 (1997) 192–203.
[30] A. Fantetti, L.R. Tamatam, M. Volvert, I. Lawal, L. Liu, L. Salles, M.R.W. Brake, C. W. Schwingshackl, D. Nowell, The impact of fretting wear on structural dynamics: experiment and simulation, Tribol. Int. 138 (2019) 111–124.
[31] S. Fouvry, P. Kapsa, L. Vincent, Quantification of fretting damage, Wear 200 (1996) 186–205.
[32] R.D. Mindlin, H. Deresiewicz, Elastic spheres in contact under varying oblique forces, J. Appl. Mech. 20 (1953).
[33] J. Ding, I.R. McColl, S.B. Leen, P.H. Shipway, A finite element based approach to simulating the effects of debris on fretting wear, Wear 263 (2007) 481–491.
[34] L. Vincent, Y. Berthier, A. Floquet, M. Godet, Fretting: load carrying capacity of wear debris, J. Tribol. 106 (1984) 192–200.
[35] S. Heredia, S. Fouvry, Introduction of a new sliding regime criterion to quantify partial, mixed and gross slip fretting regimes: correlation with wear and cracking processes, Wear 269 (2010) 515–524.
[36] O. Vingsbo, S. Söderberg, On fretting maps, Wear 126 (1988) 131–147.
[37] G.W. Stachowiak, A.W. Batchelor, Engineering Tribology, 2005.
[38] S. Mischler, Triboelectrochemical techniques and interpretation methods in tribocorrosion: a comparative evaluation, Tribol. Int. 41 (2008) 573–583.
[39] H. Dong, Tribological Properties of Titanium-based Alloys, Woodhead Publishing Limited, 2010.
[40] C. Jun, Corrosion wear characteristics of TC4, 316 stainless steel, and Monel K500 in artificial seawater, RSC Adv. 7 (2017) 23835–23845.
[41] M.Q. Neto, W.M. Rainforth, Effect of potential and microstructure on the tribocorrosion behaviour of Beta and near Beta ti alloys I, Biotribology 24 (2020), 100141.
[42] W. Xu, A. Yu, X. Lu, M. Tamaddon, L. Ng, M. Dilawer Hayat, M. Wang, J. Zhang, X. Qu, C. Liu, Synergistic interactions between wear and corrosion of Ti-16Mo orthopedic alloy, J. Mater. Res. Technol. 9 (2020) 9996–10003.
[43] J. Geringer, A. Boyer, S. Ehsani, V. Fridrici, P. Kapsa, K. Thorwarth, R. Hauert, T. Taylor, L. Semeste, P. Olubambi, New representative master curve in tribocorrosion, applications on trunnion issue, hip joint (paper-ID: 292821). Virtual EUROCORR, 2020.
[44] R.W. Neu, Progress in standardization of fretting fatigue terminology and testing, Tribol. Int. 44 (2011) 1371–1377.
[45] L. Ma, K. Eom, J. Geringer, T. Jun, Literature review on fretting wear and contact mechanics of tribological coatings, Coatings 9 (2019) 1–20.
[46] P. Corne, P. De March, F. Cleymand, J. Geringer, Fretting-corrosion behavior on dental implant connection in human saliva, J. Mech. Behav. Biomed. Mater. 94 (2019) 86–92.
[47] S. Cao, S. Mischler, Modeling tribocorrosion of passive metals – a review, Curr. Opin. Solid State Mater. Sci. 22 (2018) 127–141.